

Cosmology from weak lensing peaks and minima with Subaru Hyper Suprime-Cam survey first-year data

Gabriela A. Marques,^{1,2,3*} Jia Liu,⁴ Masato Shirasaki,^{5,6} Leander Thiele,⁷ Daniela Grandón,⁸ Kevin M. Huffenberger,³ Sihao Cheng,⁹ Joachim Harnois-Déraps,¹⁰ Ken Osato,^{11,12,13} William R. Coulton¹⁴

¹Fermi National Accelerator Laboratory, P. O. Box 500, Batavia, IL 60510, USA

²Kavli Institute for Cosmological Physics, University of Chicago, Chicago, IL 60637, USA

³Florida State University, 77 Chieftan Way, Tallahassee, FL 32306, USA

⁴Center for Data-Driven Discovery, Kavli IPMU (WPI), UTIAS, The University of Tokyo, Kashiwa, Chiba 277-8583, Japan

⁵National Astronomical Observatory of Japan (NAOJ), National Institutes of Natural Sciences, Osawa, Mitaka, Tokyo 181-8588, Japan

⁶The Institute of Statistical Mathematics, Tachikawa, Tokyo 190-8562, Japan

⁷Department of Physics, Princeton University, Princeton, NJ 08544, USA

⁸Grupo de Cosmología y Astrofísica Teórica, Departamento de Física, FCFM, Universidad de Chile, Blanco Encalada 2008, Santiago, Chile

⁹Institute for Advanced Study, 1 Einstein Dr, Princeton, NJ 08540, USA

¹⁰School of Mathematics, Statistics and Physics, Newcastle University, Herschel Building, NE1 7RU, Newcastle-upon-Tyne, UK

¹¹Center for Frontier Science, Chiba University, 1-33 Yayoicho, Inage, Chiba 263-8522, Japan

¹²Department of Physics, Graduate School of Science, Chiba University, 1-33 Yayoicho, Inage, Chiba 263-8522, Japan

¹³Kavli Institute for the Physics and Mathematics of the Universe, The University of Tokyo Institutes for Advanced Study,

5-1-5 Kashiwanoha, Kashiwa, Chiba 277-8583, Japan

¹⁴Center for Computational Astrophysics, Flatiron Institute, 162 5th Avenue, New York, NY 10010 USA

Accepted XXX. Received YYY; in original form ZZZ

ABSTRACT

We present cosmological constraints derived from peak counts, minimum counts, and the angular power spectrum of the Subaru Hyper Suprime-Cam first-year (HSC Y1) weak lensing shear catalog. Weak lensing peak and minimum counts contain non-Gaussian information and hence are complementary to the conventional two-point statistics in constraining cosmology. In this work, we forward-model the three summary statistics and their dependence on cosmology, using a suite of N -body simulations tailored to the HSC Y1 data. We investigate systematic and astrophysical effects including intrinsic alignments, baryon feedback, multiplicative bias, and photometric redshift uncertainties. We mitigate the impact of these systematics by applying cuts on angular scales, smoothing scales, statistic bins, and tomographic redshift bins. By combining peaks, minima, and the power spectrum, assuming a flat- Λ CDM model, we obtain $S_8 \equiv \sigma_8 \sqrt{\Omega_m}/0.3 = 0.810^{+0.022}_{-0.026}$, a 35% tighter constraint than that obtained from the angular power spectrum alone. Our results are in agreement with other studies using HSC weak lensing shear data, as well as with Planck 2018 cosmology and recent CMB lensing constraints from the Atacama Cosmology Telescope and the South Pole Telescope.

Key words: Weak lensing – Non-Gaussian statistics – Peak counts – Minimum counts

1 INTRODUCTION

Weak gravitational lensing (WL) is a powerful method to decode the imprints left by dark energy and dark matter in the large-scale structure (LSS). This effect arises from the coherent distortion of shapes of background galaxies by the intervening matter. The measurement of the two-point correlation function or the angular power spectrum of the weak lensing signal, known as cosmic shear, is particularly sensitive to the structure growth parameter, denoted as $S_8 \equiv \sigma_8 \sqrt{\Omega_m}/0.3$. Here, Ω_m is the total matter density today, and σ_8 represents the linear matter fluctuation on a $8h^{-1}$ Mpc scale.

Recent cosmic shear results from stage-III surveys¹, such as the Kilo Degree Survey (KiDS; Hildebrandt et al. 2020; Asgari et al. 2021; Loureiro et al. 2022), Dark Energy Survey (DES; Abbott et al. 2022; Amon et al. 2022; Secco et al. 2022), and the Subaru Hyper Suprime-Cam (HSC; Hikage et al. 2019; Hamana et al. 2020; Dalal et al. 2023; Li et al. 2023) have demonstrated their effectiveness in constraining cosmological information. However, the results have revealed a slight ($\approx 2\sigma$) discrepancy between the value of S_8 constrained from some of these analyses and that inferred from primordial cosmic microwave background (CMB) and CMB lensing measurements (Aghanim et al. 2020a,b; Bianchini et al. 2020; Qu

¹ Definition introduced by the Dark Energy Task Force report (Albrecht et al. 2006).

* gmarques@fnal.gov

et al. 2023; Madhavacheril et al. 2023). Moreover, similar disagreements have been reported in some other studies using various LSS probes (e.g., Aghanim et al. 2020b; García-García et al. 2021; White et al. 2022; Marques et al. 2023). Additional investigations are necessary to discern if the disagreements in S_8 are caused by systematic effects, statistical fluctuation, or possibly new physics yet to be understood.

The weak lensing field contains non-Gaussian (NG) features resulting from the gravitational collapse of structures, structure merging, and other astrophysical processes. To fully leverage these NG features for cosmological constraints, NG statistics are required. In addition, NG statistical tools are useful for cross-validating two-point statistics for potential systematics as they often affect two-point and NG statistics differently. Various WL NG statistics have been studied in the past, such as moments (Petri et al. 2015; Gatti et al. 2020), Minkowski functionals (Marques et al. 2019; Grewal et al. 2022), probability distribution function (Munshi & Jain 2000; Bernardeau & Valageas 2000; Liu & Madhavacheril 2019; Boyle et al. 2021; Thiele et al. 2023; Uhlemann et al. 2023), three-point statistics (Takada & Jain 2003; Semboloni et al. 2010; Fu et al. 2014), and deep learning (Fluri et al. 2019, 2022; Lu et al. 2023). In particular, the local maxima and minima on convergence maps are associated with massive halos and emptiest regions (voids) in our universe. The study of such *peaks* and *minima* is highly sensitive to nonlinear structures and a complementary probe to constrain S_8 (Liu et al. 2014a, 2015; Kacprzak et al. 2016; Shan et al. 2018; Martinet et al. 2018; Coulton et al. 2020; Harnois-Déraps et al. 2021; Zürcher et al. 2022; Liu et al. 2023).

This work presents the cosmological constraints derived from the angular power spectrum, peak counts, and minimum counts of the HSC weak-lensing first-year data (HSC Y1), which is the current data from this survey that is publicly available. To model the statistics, we adopt a forward modelling approach utilizing a large set of N -body simulations that incorporate the properties of the HSC Y1 data.

Our paper is structured as follows. In Section 2 we describe the HSC Y1 data. In Section 3, we provide a description of the simulations in the forward-modeling approach. In Section 4, we describe the method for various elements of the analysis. In Section 5 we study the impact of different astrophysical and systematic effects on our results and present null tests. Finally, we present the results and internal consistency tests in Section 6, followed by the conclusions in Section 7.

2 HSC Y1 WEAK LENSING

2.1 Shape catalog

The HSC first-year shear catalog (Mandelbaum et al. 2018a) (hereafter HSC Y1) is based on observations taken from March 2014 to April 2016 using the Subaru Hyper Suprime-Cam in five broadbands, *grizy*. The HSC Y1 is defined with conservative cuts to select galaxies with secure shape measurements, $S/N \geq 10$ and $i < 24.5$, resulting in a sample covering 136.9 deg^2 of the sky in 6 disjoint patches: XMM, GAMA09H, WIDE12H, GAMA15H, VVDS, and HECTOMAP.

The shapes $\mathbf{e} = (e_1, e_2)$ of the galaxies are estimated on the i -band coadded images using the re-Gaussianization PSF correction method (Hirata & Seljak 2003). In addition, the HSC Y1 catalog also provide quantities to calibrate the galaxy ellipticities and to compute the corresponding shear: the intrinsic shape root mean square per component ϵ_{rms} , the galaxy weight w , the additive bias $\mathbf{c} = (c_1, c_2)$, and multiplicative bias m . More information about the estimate of

z -range	N_{gal}	$n_g^{\text{eff},1} [\text{arcmin}^{-2}]$	$n_g^{\text{eff},2} [\text{arcmin}^{-2}]$
0.3 < z < 0.6	2655624	5.14	4.92
0.6 < z < 0.9	2700252	5.23	4.93
0.9 < z < 1.2	2032034	3.99	3.61
1.2 < z < 1.5	1175188	2.33	2.00

Table 1. Summary of the four HSC Y1 tomographic bins, each defined by the photometric redshift range z -range. N_{gal} is the total number of source galaxies. The effective number densities $n_g^{\text{eff},1}$ and $n_g^{\text{eff},2}$ as defined in Eqs. (1) and (2), respectively. The highest photo- z bin (shown in grey) is removed from our analysis due to systematics.

the shape catalog and its associated quantities can be found in Mandelbaum et al. (2018a) and Mandelbaum et al. (2018b).

The galaxy redshifts are determined from the HSC five broadband photometry using several independent codes (Tanaka et al. 2018). For our analysis, we restrict the source redshift range to $0.3 < z_{\text{best}} < 1.5$, where z_{best} is the best-fit photo- z determined by MLZ code. The redshift range is chosen to fall within the range deemed to be accurate by the HSC team. In Section 5.1 we check the robustness of the results when considering the photo- z estimated by two additional photo- z codes, the classical template fitting code (Mizuki) and a hybrid code combining machine learning with template fitting (Frankenz). We apply a tomography analysis by splitting the galaxy sample into four photo- z bins, with bin edges [0.3, 0.6, 0.9, 1.2, and 1.5]. However, we exclude the highest redshift bin from our analysis due to indications of unknown systematics detected prior to unblinding. Table 2.1 summarizes the properties of the individual tomographic bins, where N_{gal} is the number of source galaxies. $n_g^{\text{eff},1}$ and $n_g^{\text{eff},2}$ are the effective number densities as defined in Heymans et al. (2012) and Chang et al. (2013), respectively:

$$n_g^{\text{eff},1} = \frac{1}{\Omega_{\text{sky}}} \frac{(\sum_i w_i)^2}{\sum_i w_i^2}, \quad (1)$$

$$n_g^{\text{eff},2} = \frac{1}{\Omega_{\text{sky}}} \sum_i \frac{e_{\text{rms}}^2}{\sigma_{e,i}^2 + e_{\text{rms},i}^2}. \quad (2)$$

2.2 Reconstruction of the convergence field

The shear of each galaxy $\gamma_\alpha^{\text{obs}}$ ($\alpha = 1, 2$) is estimated from the measured ellipticity as

$$\gamma_\alpha^{\text{obs}} = \frac{1}{1 + m_{\text{tot}}} \left(\frac{e_\alpha}{2\mathcal{R}} - c_\alpha \right). \quad (3)$$

The shear responsivity \mathcal{R} —the response of the average galaxy ellipticity to a small shear distortion (Bernstein & Jarvis 2002)—is given by

$$\mathcal{R} \equiv 1 - \frac{\sum_i w_i \epsilon_{\text{rms},i}^2}{\sum_i w_i}, \quad (4)$$

where the subscript i runs over all source galaxies.

The total multiplicative bias m_{tot} includes multiplicative biases in individual galaxy's shear estimation $\langle m \rangle_i$ and two additional terms arising from galaxy size selection and redshift-dependent responsivity corrections, m_{sel} and $m_{\mathcal{R}}$, respectively (Mandelbaum et al. 2018b),

$$m_{\text{tot}} \equiv \langle m \rangle_i + m_{\text{sel}} + m_{\mathcal{R}}. \quad (5)$$

The m_{sel} and $m_{\mathcal{R}}$ multiplicative biases are estimated considering a weighted average over the ensemble of galaxies in each tomographic bin. Specifically, $10^2 m_{\text{sel}} = [0.86, 0.99, 0.91, 0.91]$ and $10^2 m_{\mathcal{R}} = [0.0, 0.0, 1.5, 3.0]$ in increasing order of redshift bins (Hikage et al. 2019; Mandelbaum et al. 2018b).

We create the pixelized shear maps, denoted as $\hat{\gamma}(\theta)$, for each of six HSC fields as

$$\hat{\gamma}(\theta) = W(\theta)\gamma^{\text{obs}}(\theta). \quad (6)$$

Here, $W(\theta)$ represents the survey mask, which is defined as the sum of the shear weights in each pixel. To construct the maps, we consider a regular flat grid with a pixel size of 0.88 arcmin and apply zero-padding beyond the boundary of the image.

The shear maps are then smoothed using the Gaussian kernel W_G , defined as

$$W_G(\theta) = \frac{1}{\pi\theta_s^2} \exp\left(-\frac{\theta^2}{\theta_s^2}\right). \quad (7)$$

Initially, we consider different values for the smoothing scale θ_s , including 1, 2, 4, 5, 8, and 10 arcmin. However, to mitigate biases due to baryonic physics, we limit the analysis of peak and minimum counts to maps smoothed with $\theta_s = 4$ arcmin and $\theta_s = 8$ arcmin (see detailed discussions in Section 5.3). For the power spectrum, we use maps smoothed with $\theta_s = 1$ arcmin and apply scale cuts. In Section 6.2, we examine the impact of different smoothing scales on cosmological constraints.

We convert the shear field into a lensing convergence field following the Kaiser–Squires inversion method (Kaiser & Squires 1993, KS),

$$\tilde{\kappa}(\ell) = \left(\frac{\ell_1^2 - \ell_2^2}{\ell_1^2 + \ell_2^2}\right)\tilde{\gamma}_1(\ell) + 2\left(\frac{\ell_1\ell_2}{\ell_1^2 + \ell_2^2}\right)\tilde{\gamma}_2(\ell), \quad (8)$$

where $\ell = (\ell_1, \ell_2)$ is the multipole, and $\tilde{\kappa}$ and $\tilde{\gamma} = (\tilde{\gamma}_1, \tilde{\gamma}_2)$ are the Fourier transforms of κ and $\hat{\gamma}$, respectively. It is well known that missing data due to survey masks may create undesirable artifacts in the KS inversion (Shirasaki et al. 2013; Liu et al. 2014b). To address this issue, we perform inpainting of the shear maps at the masked pixels using the sparsity property of the discrete cosine transform (Elad et al. 2005; Pires et al. 2009; Starck et al. 2021) before proceeding with the KS.

Finally, we obtained the smoothed convergence maps by conducting the inverse fast Fourier transform of $\tilde{\kappa}(\ell)$. The real part of the KS transformation is called an E-mode convergence map, which we simply refer to as the convergence field κ . The imaginary part, the so-called B-mode, refers to the divergence-free piece of the lensing field, which is zero in a noiseless scenario. As a result, B-mode will be used for null tests in Section 5, as it may indicate systematic effects in the data.

Following Oguri et al. (2018), we also construct a smoothed number density map of the galaxy catalog as the convolution of the number density in each pixel with the same smoothing kernel W_G . Then, we remove the pixels where this map is less than half of the mean number density since they correspond to edges and regions that are affected by bright star masks. We re-apply the smoothed masks to the convergence maps.

Fig. 1 shows the weak lensing reconstructed maps for the six HSC regions. For visualization clarity, these maps are smoothed with a Gaussian kernel on a smoothing scale of 2 arcmin. Additionally, the maps are normalized by the mean standard deviation of the convergence maps in the fiducial cosmology, as detailed in Section 3.

3 SIMULATIONS

We rely on a large set of simulation data to build an emulator, infer cosmology, and check the effect of different systematics. Here we describe the set of simulations we use to build the covariance and emulator. We describe the simulations we use to test astrophysical and systematic effects in Section 5.

3.1 Covariance training set

We use the 2268 mock realizations of the HSC Y1 shape catalogs to estimate our covariance matrix. This suite of simulations is constructed based on 108 quasi-independent full-sky N -body lensing simulations presented in Takahashi et al. (2017), with the flat- Λ CDM model cosmology consistent with the best-fit result of the Wilkinson Microwave Anisotropy Probe nine-year data (Hinshaw et al. 2013): $\Omega_b = 0.046$, $\Omega_m = 0.279$, $\Omega_\Lambda = 0.721$, $h = 0.7$, $\sigma_8 = 0.82$, and $n_s = 0.97$. The mock is built to account for observational effects in the HSC Y1 catalog, including the survey geometry, the spatial inhomogeneity of source galaxies, variations in the lensing weight, statistical noise in galaxy shape measurements, multiplicative bias, the redshifts, and distribution of the HSC galaxies. To do this, we follow the approach developed in Shirasaki & Yoshida (2014); Shirasaki et al. (2019).

The mock production can be summarized in four main steps using the information of the full-sky mocks and the observed photometric redshift, weights, shape and angular position of real galaxies:

(i) The hypothetical angular coordinates (RA and DEC) of the survey window are assigned in the full-sky mock realizations. For each of the 108 full-sky simulations, it is possible to select 21 realizations of the 6 distinct HSC fields, totalizing 2268 mock shear catalogs.

(ii) Next, each source galaxy are populated into one of the light-cone simulations, considering its original angular position and redshift. The photometric redshift information of the mocks is constructed based on MLZ method (Tanaka et al. 2018).

(iii) The ellipticities of each source galaxy, ϵ^{obs} , are randomly rotated so that the real lensing signal is erased. This done by computing $\epsilon^{\text{ran}} = \epsilon^{\text{obs}}e^{i\phi}$, where ϕ is a random number uniformly distributed between 0 and 2π . We model the intrinsic shape, ϵ^{int} , and measurement error ϵ^{mea} as:

$$\epsilon^{\text{int}} = \left(\frac{\epsilon_{\text{rms}}}{\sqrt{\epsilon_{\text{rms}}^2 + \sigma_e^2}}\right)\epsilon^{\text{ran}}, \quad \epsilon^{\text{mea}} = N_1 + iN_2, \quad (9)$$

where N_i is a random number drawn from a Gaussian distribution with a standard deviation of σ_e . The terms σ_e and ϵ_{rms} represent the shape measurement noise and the intrinsic shape dispersion per component, and are provided in the real HSC Y1 catalog as `ishape_hsm_regauss_derived_sigma_e` and `ishape_hsm_regauss_derived_rms_e`, respectively (Mandelbaum et al. 2018a).

(iv) The mock ellipticity ϵ^{mock} of each source galaxy is simulated by adding the lensing contribution at each foreground lens plane. Their components are computed as

$$\epsilon_1^{\text{mock}} = \frac{\epsilon_1^{\text{int}} + \delta_1 + (\delta_2/\delta^2)[1 - (1 - \delta^2)^{1/2}](\delta_1\epsilon_2^{\text{int}} - \delta_2\epsilon_1^{\text{int}})}{1 + \delta \cdot \epsilon^{\text{int}}} + \epsilon_1^{\text{mea}}, \quad (10)$$

$$\epsilon_2^{\text{mock}} = \frac{\epsilon_2^{\text{int}} + \delta_2 + (\delta_1/\delta^2)[1 - (1 - \delta^2)^{1/2}](\delta_2\epsilon_1^{\text{int}} - \delta_1\epsilon_2^{\text{int}})}{1 + \delta \cdot \epsilon^{\text{int}}} + \epsilon_2^{\text{mea}},$$

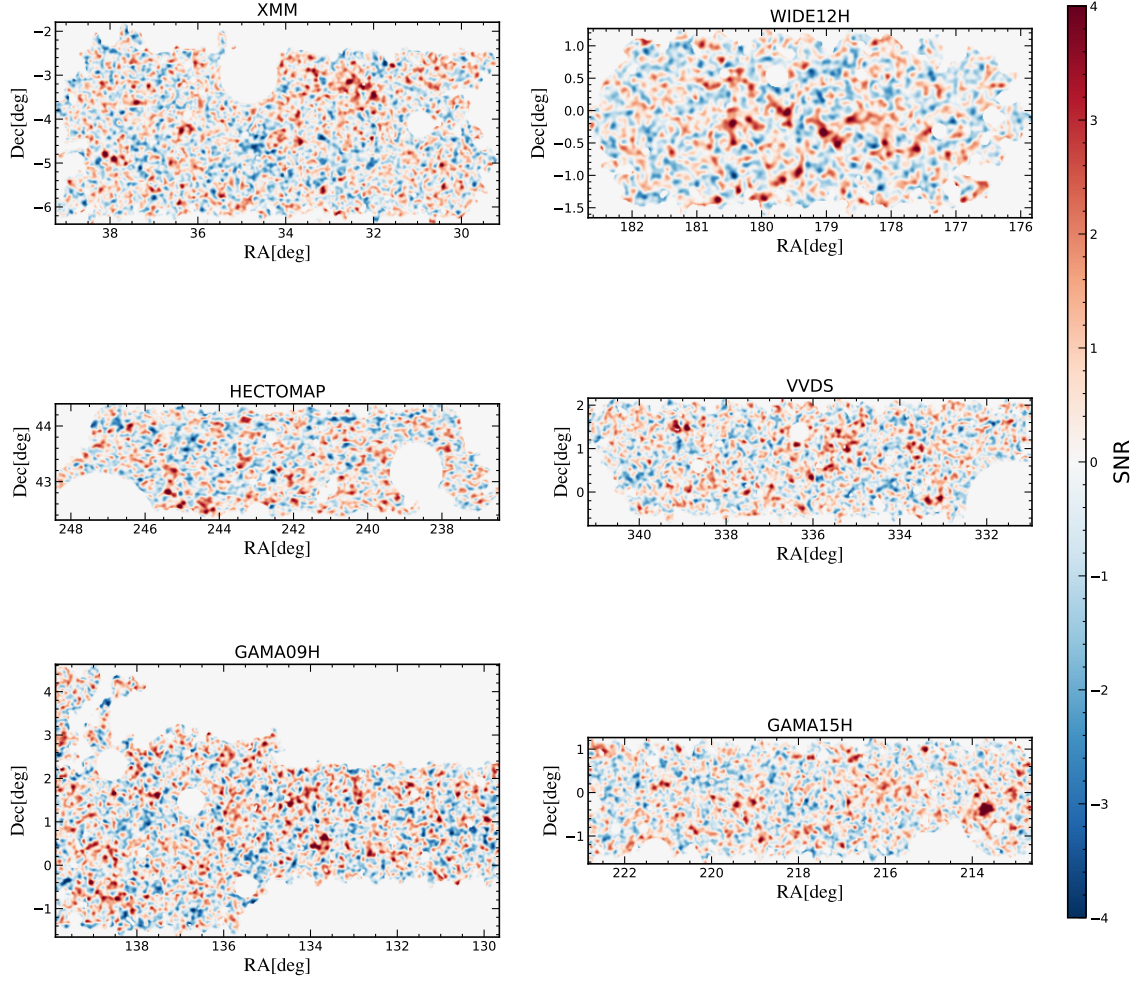


Figure 1. The reconstructed convergence fields of the six HSC Y1 regions: XMM, WIDE12H, HECTOMAP, VVDS, GAMA09H, and GAMA15H. The maps are smoothed with a Gaussian kernel on a scale of 2 arcmin for visualization purposes only. Additionally, the maps are normalized by the average standard deviation of the simulated convergence maps in fiducial cosmology. See Sections 2 and 4.1 for more details on the map-making and analysis choices.

(11)

where $\delta \equiv 2(1 - \kappa)\gamma / [(1 - \kappa)^2 + |\gamma|^2]$, and γ and κ are the simulated shear and convergence at the galaxy position of the light-cone simulation. We incorporate the multiplicative bias in the mock data by rescaling the shear values of Eqs. (10) and (11) with a factor of $\gamma \rightarrow (1 + m_{\text{tot}})\gamma$.

Finally, steps (ii)–(iv) are repeated for all the source galaxies.

3.2 Cosmology varied simulations

To perform accurate cosmological parameter inference through a forward modelling approach, it is necessary to have a reliable prediction of the summary statistics for various cosmologies. For that, we build a new set of HSC Y1 simulations with cosmology-varied based on the simulation suite introduced in Shirasaki et al. (2021). These mocks consist of ray-tracing for 100 different cosmologies in the $\Omega_m - S_8$ plane, covering $0.23 \leq S_8 \leq 1.1$ and $0.1 \leq \Omega_m \leq 0.7$. The Hubble parameter is fixed at $h = 0.6727$, the baryon density $\Omega_b h^2 = 0.02225$, dark energy equation-of-state parameter $w = -1$, and the spectral index $n_s = 0.9645$.

The N -body simulations were produced using the parallel Tree-Particle Mesh code Gadget-2, with 512^3 particles. Varying volumes

were employed to cover a broad range of redshifts, as well as have higher mass and enough spatial resolutions at lower redshifts (see Sato et al. 2009; Shirasaki et al. 2021). A typical value of the thickness of the mass sheet is about 150, 200, and $300 h^{-1} \text{Mpc}$ at $z < 0.5$, $0.5 < z < 1$, and $1 < z < 2$, respectively. The initial conditions were generated using a parallel code developed by Nishimichi et al. (2009); Valageas, P. & Nishimichi, T. (2011). A flat-sky approximation and the multiple lens-plane algorithm (Jain et al. 2000; Hamana & Mellier 2001) were adopted to generate the ray-tracing simulations. The simulations are well converged for a wide range of multipoles and in agreement with the halofit prescription (Takahashi et al. 2012). For each cosmological model, 50 ray-tracing realizations of the underlying density field were performed by randomly shifting the simulation boxes, assuming periodic boundary conditions. Finally, the cosmology-varied simulations were generated to reproduce the properties of the real data, following the steps described in Section 3.1. Fig. 3.2 shows the distribution of the simulations in the $\Omega_m - S_8$ plane. For further details on the mock production process, we refer the reader to Shirasaki & Yoshida (2014); Shirasaki et al. (2021).

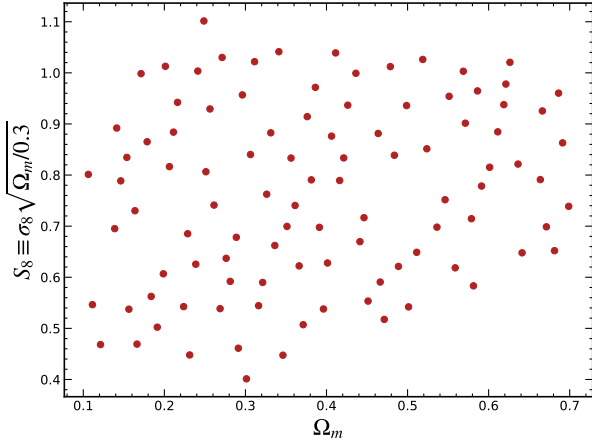


Figure 2. The distribution in the Ω_m - S_8 plane of the simulations used to build the emulator. At each point, there are 50 mock realizations.

4 METHOD

In this section, we provide an overview of the computation of summary statistics and the essential ingredients required to perform parameter inference, including emulator, covariance, and likelihood. Finally, we describe our blinding approach.

4.1 Summary statistics

In this study, we employ three statistical measures—the angular power spectrum, peak counts, and minimum counts—to extract cosmological information from the convergence maps.

The peaks are determined by identifying pixels that exhibit higher values compared to their eight neighboring pixels. We calculate the number of peaks within 19 equally-spaced bins, spanning the range of $-4 \leq \text{SNR} \leq 4$, where SNR is defined as κ/σ_0 , and σ_0 represents the mean standard deviation of the simulated convergence maps in fiducial cosmology. The choice of this range is based on previous studies that have demonstrated significant biases in peak estimates beyond $\text{SNR} > 4$ (Martinet et al. 2021). Moreover, we do not use the information from the extreme SNR bins, where the number of peaks (or minima) is less than 15. As a result, there are 11 bins for 4, arcmin and 8 bins for 8, arcmin in each tomographic bin. This cut is applied to mitigate the shot-noise contribution and to use bins where the covariance is more robust. For estimating the minimum counts, we multiply the convergence maps by -1 and follow the same procedure as for the peak counts. As described in Sections 2.2 and 5.3, we use maps smoothed with Gaussian kernels of 4 arcmin and 8 arcmin to mitigate bias resulting from baryonic feedback.

We also utilize the 2-point information provided by the power spectrum to constrain cosmology. The lensing measurement is conducted within a complex sky mask that accounts for survey partial coverage and removes artifacts such as bright stars. However, the estimation of the angular power spectrum can be biased by the mask, leading to mode coupling between different scales. To address this issue, we adopt the Pseudo- C_ℓ approach (Hivon et al. 2002) implemented by NaMaster (Alonso Monge et al. 2019), which mitigates the masking effect in the angular power spectrum estimation. Following Hikage et al. (2019), we compute the power spectrum in 14 logarithmically spaced bins, from $80 < \ell < 6500$. However, in our analysis, we use the multipole range of $300 < \ell < 1000$. The lower limit is established based on Oguri et al. (2018), where it was found that there

are unmodeled systematic errors on scales $\ell \lesssim 300$, while ℓ_{max} is defined based on possible bias due to baryons (see Section 5.3). We do not subtract the shot-noise contribution from the $C_\ell^{\kappa\kappa}$ term, as the parameter inference relies on simulations that incorporate matching noise levels. We check the validity of this assumption during one of the blinding steps, as described in Section 5.5.

For each of the 3 tomographic bins, we measure the summary statistics of each individual HSC Y1 field. We combine the power spectrum into a single array taking the weighted average of the 6 fields, using $\sum_i w_i$ as the weights of each field. The total peak and minimum counts are obtained by summing the results of each field.

4.2 Emulator

To model the summary statistics for a given cosmology, we construct an emulator based on the outcomes of cosmology-varied simulations. To achieve this, we utilize the Gaussian Process Regression (GPR) implemented in `scikit-learn`². Specifically, for modelling the peaks and minima, we utilize a Radial-Basis-Function with a fixed length of 6.1. For the power spectrum, we employ a Radial-Basis-Function with a fixed length of 1.0.³ An individual Gaussian Process Regression (GPR) emulator is trained for each element of the data vectors. In Appendix A we assess the accuracy of the emulator using a “leave-one-out” validation technique. This analysis demonstrates that the emulator is capable of recovering the input statistic at a level of a few percent, which is sufficient to obtain unbiased results.

Fig. 3 shows the sensitivity of the summary statistics for different S_8 values. For clarity, we display peaks (upper panel) and minimum counts (middle panel) for the maps smoothed with 4 arcmin only. The power spectrum of each of the tomographic bins is displayed in the lower panel.

4.3 Covariance

We use a set of $N_r = 2268$ map realizations at the fiducial cosmology to compute the covariance matrix,

$$C_{ij} = \frac{1}{N_r - 1} \sum_{n=1}^{N_r} (D_i^n - \hat{D}_i)(D_j^n - \hat{D}_j), \quad (12)$$

where D_i^n is the measurement of i -th data component in the n -th sample, and \hat{D}_i is the mean measurement of the i -th component. Here, the statistical descriptor can be the power spectrum, peak, minimum, or a combination of them in the case of the joint analysis. Figure 4 shows the correlation matrix between the power spectrum, peak counts, and minimum counts, for the 3 tomographic bins and smoothing scales of our analysis. We see positive (and negative) off-diagonal terms for the statistics, within their self-blocks and among them, which we include in the analysis.

4.4 Data compression

We implement the MOPED data compression to our data, to reduce the noise of the covariance matrix and Gaussianize the likelihood, particularly when dealing with multiple statistics, making the analysis

² <https://scikit-learn.org>

³ These values were established as optimal in the “leave-one-out” validation of the pipeline.

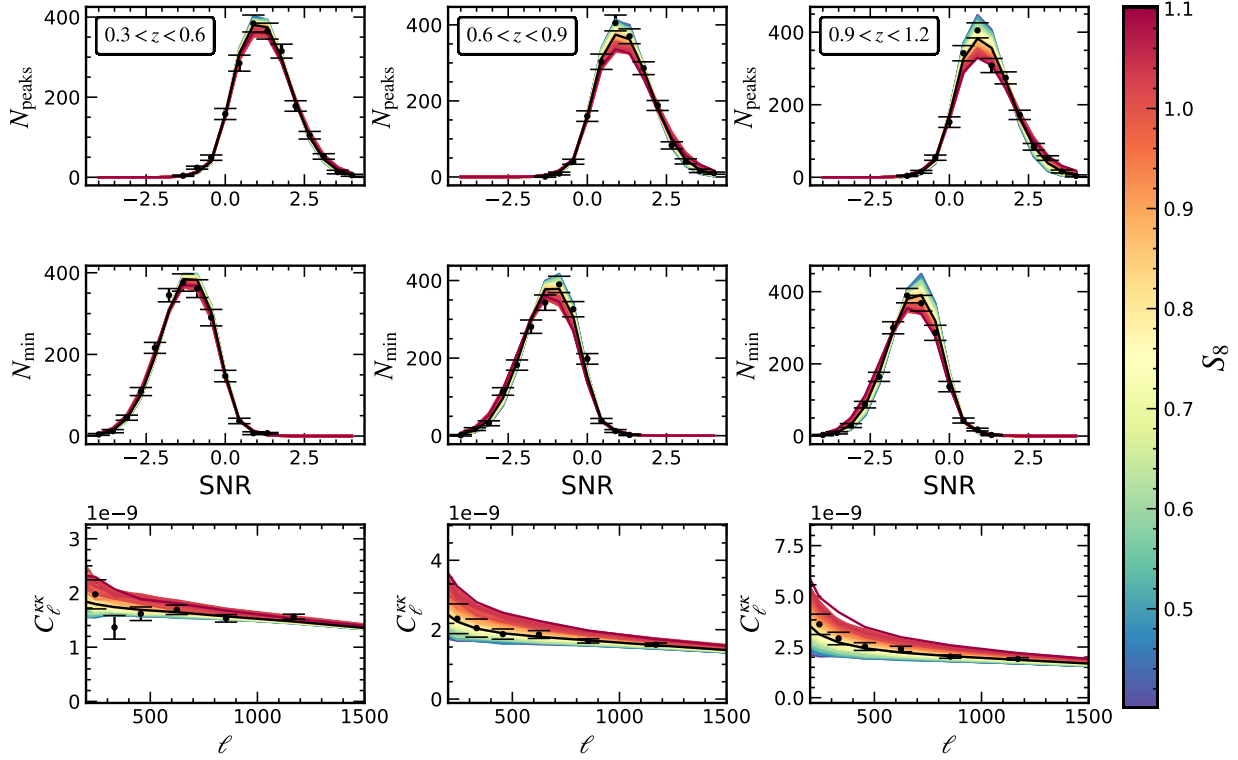


Figure 3. Peak counts (upper panel), minimum counts (middle panel) and power spectrum (lower panel) predicted for different S_8 values using the emulator. The black data points represent the measured statistics from the HSC Y1 data, and the error bars indicate the standard deviation estimated from the simulations at the fiducial cosmology. The black line denotes the predicted statistics for the best-fit parameters. For the sake of brevity, we only present the results for a smoothing scale of 4 arcmin for peaks and minima. The 8 arcmin smoothing is qualitatively similar.

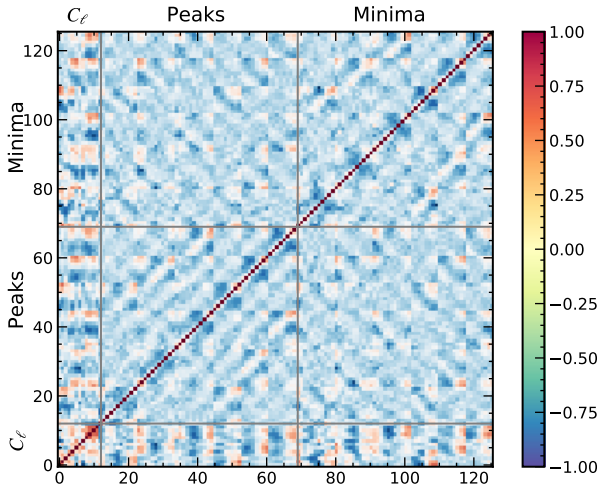


Figure 4. Correlation matrix of the peak counts, minimum counts, and power spectrum for the 3 tomographic bins. For each tomographic bin combination of the peaks and minima, we use the results of maps smoothed with 4 and 8 arcmin. The off-diagonal terms showing non-trivial correlation are also included in our parameter inference.

more computationally efficient while preserving essential cosmological information (Heavens et al. 2000; Gatti et al. 2020; Zürcher et al.

2022). The compressed data vector (D^{compr}) is computed as

$$D^{\text{compr}} = \frac{\partial D^{\text{T}}}{\partial p_m} C^{-1} D, \quad (13)$$

where $\frac{\partial D}{\partial p_m}$ represents the partial derivative of the model data vector with respect to the m -th parameter, computed using the GPR emulator. We apply the Anderson–Hartlap factor correction (Hartlap et al. 2007) when inverting the covariance matrix C^{-1} , to ensure an unbiased estimate. The MOPED procedure reduces the dimension of the uncompressed data vector D to the number of model parameters considered (in our case, Ω_m and S_8). Consequently, the compressed data vector exhibits a more Gaussian distribution, as predicted by the central limit theorem (Heavens et al. 2017; Gatti et al. 2020).

Because we discard bins outside $300 < \ell < 1000$, the power spectrum data vector comprises only 4 bins for each tomography bin, and its distribution is known to be nearly Gaussian. Consequently, we choose not to apply any data compression to the power spectrum. However, for peak and minimum counts, as well as when conducting a joint analysis (peak counts+ minimum counts+ power spectrum), we employ MOPED data compression method. We consistently apply the same data compression to the theoretical prediction when performing cosmological inference.

4.5 Parameter Inference

We perform the cosmological parameter inference, in which we evaluate the posterior of the parameters assuming a Gaussian likelihood

\mathcal{L} as

$$\ln \mathcal{L}(\mathbf{D}|\boldsymbol{\theta}) = -\frac{1}{2}[\mathbf{D} - x(\boldsymbol{\theta})]^T \mathbf{C}^{-1} [\mathbf{D} - x(\boldsymbol{\theta})] + \text{const.}, \quad (14)$$

where \mathbf{D} is the measured data vector, $x(\boldsymbol{\theta})$ is the theoretical emulator prediction at parameter values $\boldsymbol{\theta}$, and \mathbf{C} is the covariance matrix computed from the fiducial simulations.

We sample the likelihood using the Monte Carlo Markov Chain (MCMC) sampler, implemented in the publicly available code Cobaya⁴ (Lewis 2013; Torrado & Lewis 2019). We consider a flat prior on $0.1 < \Omega_m < 0.4$ and $0.5 < S_8 < 1.0$, both well covered by the cosmology-varied simulations and accurate emulator. We sample the likelihood in terms of the parameter S_8 , instead of σ_8 to obtain a uniform prior.

4.6 Blinding Strategy

In order to avoid confirmation bias, we implement a blinding approach throughout our analysis. Since the HSC Y1 data and results based on the 2-point correlation information were already unblinded in previous studies (Hamana et al. 2020; Hikage et al. 2019), we follow the steps outlined below as an honour system:

(i) Pipeline development and validation: We constructed our pipeline, including map-making, emulator, covariance, and likelihood, based solely on simulations. To validate the pipeline, we used the results of the simulation as the data array and ensured that we consistently recovered the input cosmology for all the models considered within the prior.

(ii) Analysis choices: We selected scale cuts, smoothing scales, and analysis choices based on the evaluation of systematic effects, as detailed in Section 5. Our criterion to establish the scale cuts and smoothing scales in the pipeline was chosen so that the bias introduced by systematics on S_8 was smaller than 0.3σ , as presented in Section 5.

(iii) B-mode unblinding stage: We compared the B-mode results of the fiducial mocks with the summary statistics of the B-modes of the real data. We expect both signals to exhibit noise-like behaviour. Therefore, confirming their consistency provided further confidence that our simulations accurately represent the noise levels present in the data. See Section 5.5.

(iv) Power spectrum unblinding stage: We compared the power spectrum results with those presented in Hikage et al. (2019) and Hamana et al. (2020). On the other hand, we observed a discrepancy between our results and those of the aforementioned studies when including the highest redshift bin, but consistent when using only the first three bins. A little bit after, the HSC Y3 cosmic shear analyses by Dalal et al. (2023); Li et al. (2023) were submitted, which indicated a potential bias in the highest redshift bin due to a lack of photometric redshift calibration. Consequently, we decided to exclude the highest redshift bin from our analysis to ensure the reliability and robustness of our results.

(v) Final NG statistics unblinding stage: Once we passed the previous stages, we unblinded the data vectors of peak and minimum counts and performed inferences on NG statistics as well as the joint analysis with the power spectrum.

Initially, our simulations only accounted for the first term of the total multiplicative bias as defined in Eq. (5). However, after unblinding, we discovered that, although sub-dominant, the m_{sel} and $m_{\mathcal{R}}$ terms

needed to be incorporated in order to accurately correct the total multiplicative biases of the data (Hikage et al. 2019; Hamana et al. 2020). Consequently, we updated our simulations to account for the complete correction and treated the data accordingly. It is important to note that this modification does not significantly impact our results (shift of $\sim 0.03\sigma$ on S_8), as the amplitudes of these terms are relatively small. Nonetheless, we present our results after accounting for these changes.

Before incorporating the total multiplicative bias, the smaller smoothing scales considered in the map production were 1, 2, and 5 arcmin. Given these configurations, it was observed that in order to obtain unbiased results due to baryonic feedback, for both peak and minimum counts, the minimum scale required was 5 arcmin. However, when producing the mocks with the total multiplicative bias, additional smoothing scales were examined, and it was found that including a smoothing scale of 4 arcmin was also effective in obtaining unbiased results when appropriate cuts were applied. Considering the goal of optimizing the constraining power and capturing the non-Gaussian information of the maps, we adopt the smoothing scales of 4 and 8 arcmin in our baseline setup to achieve the best possible performance in the cosmological analysis.

5 SYSTEMATICS AND NULL-TESTS

In this section, we examine the impact of various systematic and astrophysical effects on our results, including photometric redshift uncertainties, image calibration uncertainties, baryonic feedback, and galaxy intrinsic alignment. To assess the impact of these effects, we conducted parameter inference for different analysis choices using distinct mocks specifically designed to simulate each effect, as described below in Sections 5.1-5.4. In this process, we replaced the synthetic data vector at the fiducial cosmology with another synthetic data vector that was contaminated with each of these systematics. Our goal was to analyze the shifts in S_8 resulting from these substitutions, allowing us to understand the consequences of any mis-modelling of these effects. The necessary scale cuts and smoothing scales in our pipeline are defined ensuring that any shifts in S_8 with respect to the constraints of the fiducial, uncontaminated mocks remain below 0.3σ .

Fig. 5 shows the shift on S_8 with respect to the constraints from the fiducial cosmology for each systematic. We show the results corresponding to our baseline setup, which includes the power spectrum with $300 < \ell < 1000$ and peak counts jointly with minimum counts of maps smoothed with 4 arcmin and 8 arcmin, while also excluding extreme bins with counts less than 15. For the baseline setup, all systematics introduce biases that are smaller than our predefined acceptable criterion for this analysis. Therefore, we proceed with the analysis by applying the necessary cuts, rather than marginalizing over these effects. This reinforces the reliability of our parameter estimation, demonstrating that the baseline setup is robust against the considered systematics. However, it is worth noting that a full error propagation of the uncertainties in shape calibration, photo- z , baryons, and IA achieved through marginalization over nuisance parameters would consistently result in larger error bars for all statistics.

For all the effects we investigated, we observed that baryons had the most significant impact on causing shifts in S_8 when considering smaller scales. Specifically, for the baryonic feedback in an HSC-like survey, we found that the maps should be smoothed with smoothing scales larger than 4 arcmin, and we should limit the power spectrum analysis to $\ell < 1000$ in order to get unbiased results according to our criterion. A further study of the impact of baryonic feedback using

⁴ <https://cobaya.readthedocs.io/en/latest/index.html>

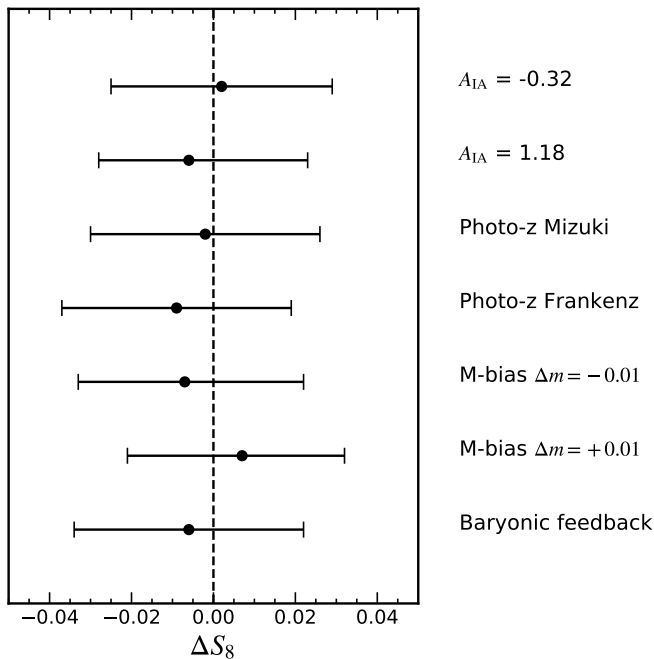


Figure 5. Impact of systematic effects on S_8 constraints considering the analysis choices of our baseline analysis. We use simulations to check the expected shifts on S_8 , including baryonic feedback mechanisms, intrinsic alignments, and uncertainties of photometric redshifts and of the multiplicative bias.

different models in these NG statistics for the HSC data is explored in [Grandón et al. \(2023\)](#).

In addition, we conduct a null test in Section 5.5 by comparing the B-mode maps from real data with those generated from our mocks. More details about the method, results, and simulations used to perform these tests are described below.

5.1 Photometric redshift uncertainties

In our baseline analysis, we define the tomographic redshift bins based on the best estimation by the MLZ algorithm. To assess the impact of photo- z uncertainties on our results, we generate 100 additional HSC Y1 realizations of the fiducial model by adopting two alternative redshift estimates: one provided by the Mizuki and the other by the Frankenz method ([Tanaka et al. 2018](#)). For each of these two mocks, we compute the statistics and calculate their averages, which are then used as the data vector for our cosmology constraints. During the parameter inference, we utilize the emulator constructed based on the MLZ code. Given that the redshift distributions are slightly different among these methods, this test allows us to investigate and quantify any potential biases or inconsistencies that may arise from unaccounted effects associated with photo- z uncertainties.

We found that the Frankenz model causes a shift in S_8 towards negative values of 0.22σ with respect to the fiducial model, while the Mizuki model shifts it by 0.05σ . Therefore, we do not expect bias larger than the threshold established (0.3σ) in our analysis caused by different photometric redshift distributions.

5.2 Image calibration uncertainties

Our mock data are generated with a single multiplicative bias value for each field and tomographic bin. However, the HSC Y1 multiplicative bias is determined by image simulations and has an associated uncertainty at the percent level. To explore the impact of this uncertainty, we create two sets of mock data with the multiplicative bias intentionally miscalibrated by $\Delta m = \pm 0.01$. Each set consists of 100 realizations and is generated by modifying Eqs. (10) and (11) as $\gamma \rightarrow (1 + m_{\text{tot}} \pm \Delta m)\gamma$, but the mock shear catalogs are intentionally miscalibrated using only $(1 + m_{\text{tot}})$ in Eq. (3). We assess the impact of the multiplicative bias uncertainty on our parameter estimation, by employing the average of statistics of the miscalibrated mocks as the data vector. However, we utilize the emulator constructed with well-calibrated mocks to predict the theoretical values.

We found a $\Delta m = +0.01$ in our maps can bias the S_8 by 0.18σ , and by 0.17σ towards negative values for $\Delta m = -0.01$, both of which meet our criterion.

5.3 Baryonic feedback

Baryonic effects significantly suppress the matter power spectrum on small scales ([Martinet et al. 2021](#); [Ferlito et al. 2023](#)). To investigate the impact of baryons on our analysis and establish the framework for our study, we utilize the κ TNG dataset ([Osato et al. 2021](#)). This dataset is based on the cosmological hydrodynamic simulations IllustrisTNG ([Pillepich et al. 2018](#); [Nelson et al. 2019](#)). It comprises 10,000 realizations for a set including baryons (κ^{baryons}) and dark matter only (κ^{DM}). We weigh the κ TNG light cones by the HSC Y1 redshift distribution to place the source galaxies like our data. Next, we add shape noise with variance

$$\sigma^2 = \frac{\sigma_e^2}{n_g^{\text{eff},1} A_{\text{pix}}}, \quad (15)$$

where σ_e is mean intrinsic ellipticity of galaxies ($\sigma_e \sim 0.28$), $n_g^{\text{eff},1}$ is the galaxy number density in Table 2.1, and A_{pix} is the solid angle of a pixel. To investigate the scale at which the baryonic effects can be sufficiently mitigated, we apply a Gaussian smoothing filter to the maps following the same procedure as applied to the data (Eq. 7).

We compute the power spectrum, peak, and minimum of the κ^{DM} and κ^{baryons} sets. We then employ the statistics derived from the fiducial cosmology, scaled by the ratio between the hydro-simulations and the dark-matter-only results, as the data vector for parameter constraints. This allows us to quantify the shift in the $\Omega_m - S_8$ plane due to baryons under various scenarios and scale cuts.

Considering the scale cuts and smoothing scales of our baseline analysis, we found the impact of baryons on S_8 is smaller than our predefined acceptable criterion, by 0.15σ .

5.4 Galaxy intrinsic alignment

The intrinsic alignment (IA) of galaxies can lead to systematic errors in weak gravitational lensing measurements, as it introduces additional correlations in the observed shapes of galaxies.

In the context of the non-linear tidal alignment model (NLA), the strength of this effect is determined by the coupling parameter A_{IA} ([Bridle & King 2007](#)). Previous 2-pt analyses with HSC Y1 data report $A_{\text{IA}} = 0.38 \pm 0.70$ ([Hikage et al. 2019](#)), and $A_{\text{IA}} = 0.91^{+0.27}_{-0.32}$ ([Hamana et al. 2020](#)), also consistent with results using Convolutional Neural Network ($A_{\text{IA}} = 0.20^{+0.55}_{-0.58}$) ([Lu et al. 2023](#)). To study the impact of the intrinsic alignment of galaxies in our statistics, we

use the simulations presented in Harnois-Déraps et al. (2022) that contain IA physically consistent with the NLA model. To match the photometric redshift distribution in our analysis, we weigh these light cones to match the HSC photometric redshift distribution.

Based on 2-pt HSC constraints on A_{IA} , we explore the scenario with minimum and maximum values given $\pm 1\sigma$ of these results, i.e., $A_{IA} = 1.18$ and $A_{IA} = -0.32$. Following the procedure described in Harnois-Déraps et al. (2022), we multiply the $\epsilon_{1/2}^{IA}$ catalog entries by the A_{IA} amplitudes and combine with the $\gamma_{1/2}$ columns. We refer the readers to Harnois-Déraps et al. (2022) for more details on the IA mocks. We introduce shape noise to the simulations following Eq. (15), similar to the procedure used for accounting for baryonic effects.

Subsequently, similarly to the approach described in Section 5.3, we contaminate the synthetic data vector at the fiducial cosmology by multiplying it with the ratio between the results of maps with A_{IA} and $A_{IA} = 0$. This allows us to study the impact of intrinsic alignment on our parameter constraints and understand how it influences our cosmological analysis.

For $A_{IA} = 1.18$, S_8 is biased by 0.16σ towards negative values, and by 0.05σ towards positive values for $A_{IA} = -0.32$, which we deem acceptable for this analysis. It is important to note that our study does not incorporate cross-redshift bins for any of the probes. While this inclusion would likely enhance the constraining power (Harnois-Déraps et al. 2021; Zürcher et al. 2022), these cross-redshift bins are more susceptible to the impact of IA (Harnois-Déraps et al. 2022), which would likely require full modelling within the emulator.

5.5 B-mode maps

As a null test, we compare the statistics of the B-mode signals obtained from the fiducial simulations with those derived from real data. We expect that the gravitational lensing effect does not produce a divergence-free component, so both the fiducial simulations and real data B-mode maps should primarily contain pure shape noise signals. By comparing these two sets, we can verify if they exhibit consistent signals, which further strengthens our confidence in the accuracy of the noise levels of our simulations and the fidelity of our data.

To estimate the χ^2 and corresponding probability-to-exceed (PTE) between the B-mode signal observed in real data and simulations, we utilize the covariance derived from the B-modes of the fiducial simulations. The results for each scenario are presented in Table 2. We impose a requirement of PTE $> 1\%$ for the test to pass. We find consistency with the B-mode results for all statistics and redshift bins.

6 RESULTS

In this section, we present results from weak lensing statistics of the HSC Y1 data, including the angular power spectrum, peak counts, and minimum counts. The tomographic bins, scale cuts, and smoothing scales we adopted in our baseline analysis are described in Section 4.

6.1 Cosmological Constraints

In this work, we use the angular power spectrum, peak, and minimum counts of the HSC Y1 data to constrain the matter density parameter Ω_m and the combination sensitive to the structure growth, $S_8 = \sigma_8 \sqrt{\Omega_m/0.3}$.

Statistics	Photo-z bin	$\chi^2_{\text{null}}/\text{dof}$	PTE (%)
Power Spectrum	$0.3 < z < 0.6$	9.09/4	5.90
	$0.6 < z < 0.9$	4.06/4	40.51
	$0.9 < z < 1.2$	3.07/4	54.52
Peak Counts	$0.3 < z < 0.6$	11.16/13	59.73
	$0.6 < z < 0.9$	21.28/13	6.73
	$0.9 < z < 1.2$	12.16/13	56.31
Minimum Counts	$0.3 < z < 0.6$	5.14/9	82.18
	$0.6 < z < 0.9$	4.93/9	84.03
	$0.9 < z < 1.2$	7.80/9	55.37

Table 2. Summary of χ^2 per degree of freedom and the probability-to-exceed (PTE) for the null-test using B-modes of our mocks and real data.

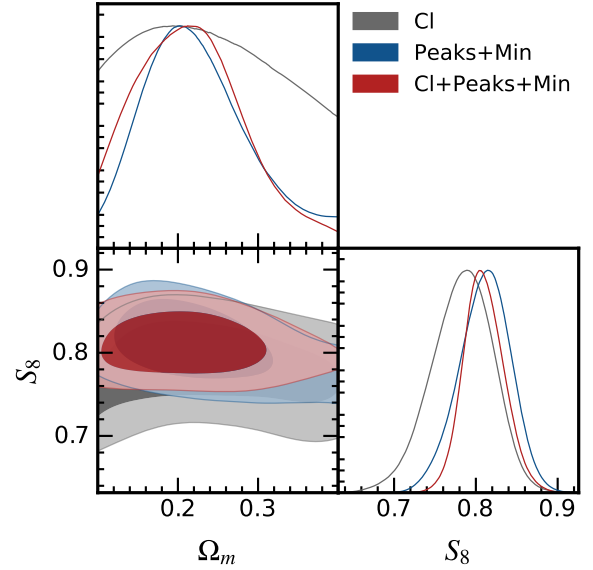


Figure 6. Constraints on the Ω_m and $S_8 \equiv \sigma_8 \sqrt{\Omega_m/0.3}$ inferred using the angular power spectra (grey contour) and the joint peak and minimum counts estimation (blue contour) of the HSC Y1 data. The red contour is the joint estimation between the three summary statistics.

In Fig. 6, we show the parameter constraints from the measured statistics in our baseline analysis. In particular, using the angular power spectrum alone (grey contour) we find

$$\begin{aligned} \Omega_m &= 0.241^{+0.059}_{-0.130}; \\ S_8 &= 0.783^{+0.040}_{-0.034}. \end{aligned}$$

Here, we report the 1D marginalized mode and the $\pm 34\%$ confidence intervals. The constraints from the combination of peak and minimum counts (blue contour of Fig. 6) yield

$$\begin{aligned} \Omega_m &= 0.225^{+0.048}_{-0.079}; \\ S_8 &= 0.811^{+0.033}_{-0.029}. \end{aligned}$$

We observe agreement for the results using the different summary statistics, although the results using NG statistics prefer slightly higher S_8 values than the power spectrum. The constraints of peaks and minima lead to a tightening of the S_8 and Ω_m constraints by approximately 16% and 32%, respectively, compared to the constraints obtained from the power spectrum alone.

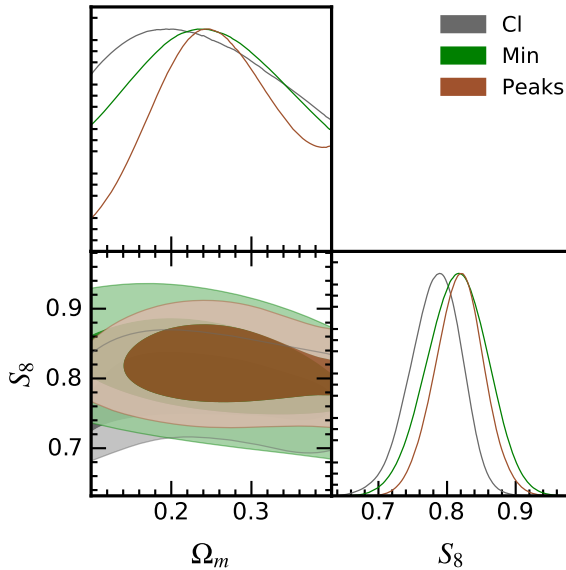


Figure 7. Cosmological constraints (1 and 2σ contours) obtained from individual summary statistics of HSC Y1 data: angular power spectrum (grey), Minimum counts (green), and Peak counts (brown).

Statistics	S_8	Ω_m	PTE [%]
C_ℓ	$0.783^{+0.040}_{-0.034}$	$0.241^{+0.059}_{-0.130}$	16.4
Peaks+Min	$0.811^{+0.033}_{-0.029}$	$0.225^{+0.048}_{-0.079}$	40.6
Peaks+Min+ C_ℓ	$0.810^{+0.022}_{-0.026}$	$0.218^{+0.053}_{-0.079}$	42.7
Peaks	0.818 ± 0.035	$0.258^{+0.073}_{-0.082}$	44.9
Min	0.815 ± 0.044	0.248 ± 0.079	47.2

Table 3. Summary of our cosmological constraints for different combinations of statistics and the corresponding probability-to-exceed (PTE).

Combining peak counts, minimum counts, and power spectrum we find

$$\begin{aligned} \Omega_m &= 0.218^{+0.053}_{-0.079}; \\ S_8 &= 0.810^{+0.022}_{-0.026}, \end{aligned}$$

with contour presented in red in Fig. 6. This joint constraint represents an improvement of 30% in Ω_m and 35% in S_8 compared to the constraints from the angular power spectrum alone. This improvement highlights the valuable contribution of peak and minimum counts in enhancing the precision of cosmological parameter constraints, which aligns with the findings from other studies (Liu et al. 2015; Harnois-Déraps et al. 2021; Zürcher et al. 2022).

The primary improvement of the NG statistics on the power spectrum constraints arises from the peak counts, as shown in Fig. 7. When utilizing peak counts alone, we obtain $\Omega_m = 0.258^{+0.073}_{-0.082}$ and $S_8 = 0.818 \pm 0.035$. For minimum counts, we find $\Omega_m = 0.248 \pm 0.079$ and $S_8 = 0.815 \pm 0.044$. We summarize our main results with the corresponding PTE for the different data combinations in Table 6.1.

Our results show consistency with previous studies that used the HSC Y1 2-point information, $S_8 = 0.780^{+0.030}_{-0.033}$ (Hikage et al. 2019), $S_8 = 0.823^{+0.032}_{-0.028}$ (Hamana et al. 2020) and $S_8 = 0.812 \pm 0.021$ (Longley et al. 2023). Recently, Dalal et al. (2023) and Li et al. (2023) conducted two-point analyses using the first three years of data of

HSC (Li et al. 2022), which covers an area increased by ~ 3 times the HSC Y1 area. The results from the Y3 analyses are in agreement with the HSC Y1 (and with our results), although the S_8 value is slightly lower: $S_8 = 0.776^{+0.032}_{-0.033}$ and $S_8 = 0.769^{+0.031}_{-0.034}$, respectively. Despite the Y3 data having significantly increased the HSC Y1 area, the constraining power in S_8 for Y3 is similar to HSC Y1 (Hikage et al. 2019; Hamana et al. 2020) due to the analysis choices adopted to mitigate biases in the photometric redshift estimates. Our results using NG statistics have demonstrated the potential to yield tighter constraints than the power spectrum alone. With this in mind, a future study using NG statistics for the Y3 data could hold the promise of further improving the precision of cosmological parameter constraints.

In the context of measurements obtained from the 2-point information of other stage-III weak lensing surveys, our results are in agreement within the 1σ level (considering the sum of the statistical uncertainties in quadrature) with many studies, including KiDS-1000 (Asgari et al. 2021; Loureiro et al. 2022), DES-Y3 (Secco et al. 2022; Amon et al. 2022; Doux et al. 2022) and KiDS-1000 plus DES Y3 combined (DES and KiDS Collaboration 2023).

Our results are consistent with other stage-III studies that use beyond the 2-point information to constrain S_8 , such as the peak counts (Zürcher et al. 2022), and the second and third moments of weak lensing DES Y3 data (Gatti et al. 2020). The S_8 constraints from KiDS-450 and KiDS-1000 data using deep learning (Fluri et al. 2019, 2022), peak counts (Martinet et al. 2018), and peak counts at high SNR (Shan et al. 2018) are also consistent with our findings. We also find a good agreement with Lu et al. (2023), which employs peak counts and convolutional neural networks to constrain cosmology with HSC Y1 data, and with Liu et al. (2023), which selected the peak counts at high SNR > 3.5 to derived the constraints using a halo-based theoretical peak model. It is important to note that the analysis choices of these studies differ from ours in many aspects, including the redshift bins, cross-correlation between the bins, data vector binning, scale cuts, simulations, treatment of systematic errors, parameters considered during the inference, and modeling of the matter power spectrum and of the summary statistics.

The analysis of the TT-TE-EE- and low-E polarization of the *Planck* satellite (*Planck* TT+TE+EE+lowE) found a higher S_8 ($S_8 = 0.834 \pm 0.016$) than the values typically found by cosmic shear analysis (Aghanim et al. 2020a). Although our result is slightly lower, we still find a good agreement with the CMB results for all combinations, including the power spectrum, peaks, and minima separately, as well as the power spectrum, peaks, and minimum jointly. We also found good agreement with the results from CMB lensing of the Atacama Cosmology Telescope (ACT) plus Baryon Acoustic Oscillations (BAO) (Madhavacheril et al. 2023; Qu et al. 2023) and from CMB lensing of the South Pole Telescope (SPT) (Bianchini et al. 2020). In Figure 8, we summarize this comparison of our S_8 constraints (red) with the results from external stage-III cosmic shear (green), primary CMB (blue), CMB lensing (teal), and stage-III results from beyond 2-point analyses (purple).

6.2 Internal consistency checks

In previous studies, HSC Y1 data have been subjected to comprehensive tests to assess various systematic and astrophysical effects (Mandelbaum et al. 2018a; Oguri et al. 2018; Hikage et al. 2019; Hamana et al. 2020; Marques et al. 2020). In addition to these previous investigations, we have examined the potential impact of the most concerning effects in our results and implemented the necessary analysis choices to mitigate them. To further ensure the robustness

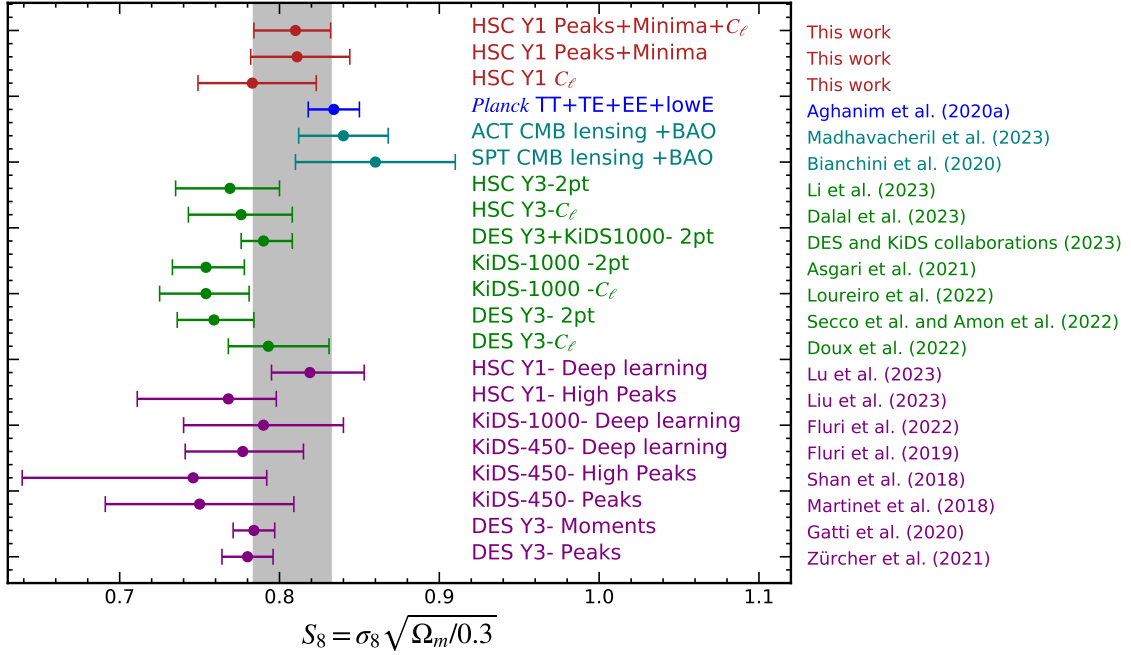


Figure 8. Comparison between our S_8 results for different statistical combinations (red points) with external studies: primary CMB (blue point), CMB lensing (teal points), and stage-III weak lensing analyses using 2-point information in real-space (“2pt”) and in harmonic space (“ C_ℓ ”) (green points). The purple points represent stage-III results from beyond 2-point analyses. We caution the reader that these results stem from distinct datasets as well as different analysis methodologies, including the cosmological and nuisance parameters, priors, model, scale cuts, systematic mitigation strategies, and other specific considerations so that the error bars can vary depending on the setup. For instance, among other differences such as the type of neural network, the results from KiDS-1000 deep learning (Fluri et al. 2022) are based on a w CDM model, while the KiDS-450 deep learning analysis (Fluri et al. 2019) utilizes a Λ CDM model.

of our results, we perform parameter constraints under the following setups:

- **Tomographic bins:** We analyze the data using each individual tomographic bin to assess the sensitivity of our results at each redshift. For this test, we jointly consider the power spectrum, minimum, and peak counts to carry out the parameter constraints.
- **Removing each tomographic bin:** Each individual redshift bin is removed from the analysis to evaluate the influence on the final cosmological constraints. For this test, we jointly consider the power spectrum, minimum, and peak counts to carry out the parameter constraints.
- **Smoothing scales:** We explore the effect of scales on our NG statistics by performing inference with maps smoothed with the various smoothing scales, including the 4, 5, 8, and 10 arcmin. For this test, we consider the combination of peak and minimum counts.
- **Power spectrum with different scale cuts:** We investigate the consequences of varying scale cuts on the angular power spectrum (Cl) to determine the sensitivity of our results to these choices. For this test, we only consider the power spectrum measurements.

In Fig. 9, we show the constraints on S_8 for the scenarios described above. We also show in red the results from our baseline setup, that is the angular power spectrum, peak, and minimum counts of the 3 tomographic bins combined, considering the scale cut of $300 < \ell < 1000$ for the power spectrum and 4 arcmin and 8 arcmin for the NG statistics. We find consistency within 1σ in all the different analysis choices, indicating the robustness of our results.

7 CONCLUSIONS

In this work, we used two non-Gaussian statistics—the peak counts and minimum counts—in addition to the conventional power spectrum, to constrain the matter density Ω_m and the structure growth parameter S_8 , assuming a flat- Λ CDM model. We found that the NG statistics, particularly the peak and minimum counts jointly, significantly tighten the cosmological constraints. Combining the angular power spectrum, peak counts, and minimum counts, we obtained 68% C.L. constraints of $\Omega_m = 0.218^{+0.053}_{-0.079}$ and $S_8 = 0.810^{+0.022}_{-0.026}$, an improvement of 30% and 35%, respectively, compared to those from the angular power spectrum alone, $\Omega_m = 0.241^{+0.059}_{-0.130}$ and $S_8 = 0.783^{+0.040}_{-0.034}$.

To achieve these results, we forward-modelled the summary statistics within our prior range of cosmological parameters, using a suite of N -body simulations that incorporate the properties of the HSC Y1 data. We tested and validated our pipeline with these simulated mocks prior to analyzing the real data. We assessed the impact of systematics such as intrinsic alignments, baryon feedback, multiplicative bias, and photometric redshift uncertainties. We performed thorough internal consistency tests, finding robust agreements across statistics, angular scales, smoothing scales, and tomographic redshift bins included in our analysis. While the strategy in this work to mitigate systematic effects involved applying scale cuts, smoothing the maps with larger scales, and not including cross-redshift bins for any of the probes, higher-precision studies require addressing the challenges of controlling systematics to robustly constrain cosmology with the information of the non-linear structure of the matter field. We expect future work will improve upon our method by forward-modelling the systematics and marginalizing them without discarding the precious

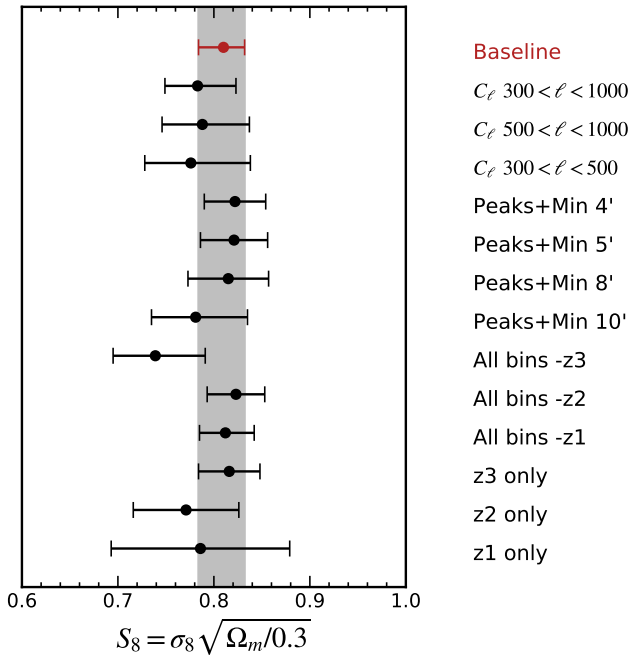


Figure 9. Constraints on S_8 and its robustness against various analysis choices described in Section 6.2. The red point highlights the results from the baseline analysis, where we combine the angular power spectrum, peak counts, and minimum counts of the 3 tomographic bins, along with a scale cut of $300 < \ell < 1000$ for the power spectrum and 4 and 8 arcmin for the NG statistics. The shaded grey area represents the 68% credible interval for the baseline constraints.

data. Our results are in broad agreement with those from previous HSC analyses and with other stage-III weak lensing analyses, using 2-point and non-Gaussian statistics, as summarized in Figure 8 and discussed in Section 6. However, while weak lensing two-point analyses have typically revealed a lower S_8 than the ones from CMB, our results are also in good agreement (within 1σ) with *Planck* and with CMB lensing results from ACT and SPT (Bianchini et al. 2020; Qu et al. 2023; Madhavacheril et al. 2023).

Our study demonstrated that weak lensing non-Gaussian statistics are not only powerful probes to tighten cosmological constraints beyond 2-point statistics, but also useful tools to investigate the origin of the so-called S_8 tension between weak lensing and CMB studies. We expect the constraints to be significantly improved with the final-year HSC dataset which will cover $\sim 1000 \text{ deg}^2$ of the sky. As the deepest large-area weak lensing survey to date, the HSC survey has provided us with a glimpse of what is expected from the forthcoming stage-IV surveys such as *Vera Rubin Observatory LSST* (Ivezic et al. 2019), *Euclid* (Laureijs et al. 2011), and *Nancy Grace Roman Space Telescope* (Spergel et al. 2015). Together, they will probe the growth of structures at unprecedented precision. Non-Gaussian statistics, such as the ones studied here, provide excellent opportunities to drive discovery in cosmology with these stage-IV surveys.

ACKNOWLEDGEMENTS

We thank Alex Drlica-Wagner, Xiangchong Li, Joaquín Armijo, Sunao Sugiyama, Masahiro Takada, Surhud More, Brian Lu, Zoltán Haiman for useful discussions. GM and KMH acknowledge support

from the National Science Foundation award 1815887 and the FSU College of Arts and Sciences Dean’s Postdoctoral Scholar Fellows program. This manuscript has been authored by Fermi Research Alliance, LLC under Contract No. DE-AC02-07CH11359 with the U.S. Department of Energy, Office of Science, Office of High Energy Physics. This work was supported by JSPS KAKENHI Grants 23K13095 and 23H00107 (to JL), 19K14767 and 20H05861 (to MS), and 21J00011 (to KO). The work of LT is supported by the NSF grant AST 2108078. DG acknowledges support from the ANID-Doctorado Nacional/2019-2119188. JHD acknowledges support from an STFC Ernest Rutherford Fellowship (project reference ST/S004858/1). We thank the Yukawa Institute for Theoretical Physics at Kyoto University, where part of the discussions of this work took place during YITP-T-22-03 on “Cosmology with Weak Lensing: Beyond the Two-point Statistics” and YITP-W-23-02 on “Future Science with CMB x LSS”. Part of this work was performed at the Aspen Center for Physics, which is supported by National Science Foundation grant PHY-1607611. We acknowledge the use of many public Python packages not cited along the main text: Numpy (Oliphant 2015), Astropy⁵ a community-developed core Python package for Astronomy (Astropy Collaboration et al. 2013; Price-Whelan et al. 2018), Matplotlib (Hunter 2007), IPython (Pérez & Granger 2007) and Scipy (Jones et al. 01). This research used computing resources at Kavli IPMU. This research used resources at the National Energy Research Scientific Computing Center (NERSC), a U.S. Department of Energy Office of Science User Facility located at Lawrence Berkeley National Laboratory, operated under Contract No. DE-AC02-05CH11231. The authors are pleased to acknowledge that the work reported in this paper was substantially performed using the Princeton Research Computing resources at Princeton University which is consortium of groups led by the Princeton Institute for Computational Science and Engineering (PICSciE) and Office of Information Technology’s Research Computing.

REFERENCES

- Abbott T., et al., 2022, *Physical Review D*, 105, 023520
Aghanim N., et al., 2020a, *Astronomy & Astrophysics*, 641, A6
Aghanim N., et al., 2020b, *Astronomy & Astrophysics*, 641, A8
Albrecht A., et al., 2006, arXiv preprint astro-ph/0609591
Alonso Monge D., Sanchez J., Slosar A., 2019, *Monthly Notices of the Royal Astronomical Society*, 484, 4127
Amon A., et al., 2022, *Physical Review D*, 105, 023514
Asgari M., et al., 2021, *Astronomy & Astrophysics*, 645, A104
Astropy Collaboration et al., 2013, *A&A*, 558, A33
Bernardeau F., Valageas P., 2000, *A&A*, 364, 1
Bernstein G., Jarvis M., 2002, *The Astronomical Journal*, 123, 583
Bianchini F., et al., 2020, *The Astrophysical Journal*, 888, 119
Boyle A., Uhlemann C., Friedrich O., Barthelemy A., Codis S., Bernardeau F., Giocoli C., Baldi M., 2021, *MNRAS*, 505, 2886
Bridle S., King L., 2007, *New Journal of Physics*, 9, 444
Chang C., et al., 2013, *Monthly Notices of the Royal Astronomical Society*, 434, 2121
Coulton W. R., Liu J., McCarthy I. G., Osato K., 2020, *Monthly Notices of the Royal Astronomical Society*, 495, 2531
DES and KiDS Collaboration 2023, arXiv e-prints, p. arXiv:2305.17173
Dalal R., et al., 2023, arXiv preprint arXiv:2304.00701
Doux C., et al., 2022, *Monthly Notices of the Royal Astronomical Society*, 515, 1942
Elad M., Starck J.-L., Querre P., Donoho D. L., 2005, *Applied and computational harmonic analysis*, 19, 340

⁵ <http://www.astropy.org>

- Ferlito F., et al., 2023, arXiv preprint arXiv:2304.12338
- Fluri J., Kacprzak T., Lucchi A., Refregier A., Amara A., Hofmann T., Schneider A., 2019, *Physical Review D*, 100, 063514
- Fluri J., Kacprzak T., Lucchi A., Schneider A., Refregier A., Hofmann T., 2022, *Physical Review D*, 105, 083518
- Fu L., et al., 2014, *Monthly Notices of the Royal Astronomical Society*, 441, 2725
- García-García C., Ruiz-Zapatero J., Alonso D., Bellini E., Ferreira P. G., Mueller E.-M., Nicola A., Ruiz-Lapuente P., 2021, *Journal of Cosmology and Astroparticle Physics*, 2021, 030
- Gatti M., et al., 2020, *Monthly Notices of the Royal Astronomical Society*, 498, 4060
- Grandón D., et al., 2023, in prep
- Grewal N., Zuntz J., Tröster T., Amon A., 2022, arXiv preprint arXiv:2206.03877
- Hamana T., Mellier Y., 2001, *Monthly Notices of the Royal Astronomical Society*, 327, 169
- Hamana T., et al., 2020, *PASJ*, 72, 16
- Harnois-Déraps J., Martinet N., Castro T., Dolag K., Giblin B., Heymans C., Hildebrandt H., Xia Q., 2021, *Monthly Notices of the Royal Astronomical Society*, 506, 1623
- Harnois-Déraps J., Martinet N., Reischke R., 2022, *Monthly Notices of the Royal Astronomical Society*, 509, 3868
- Hartlap J., Simon P., Schneider P., 2007, *Astronomy & Astrophysics*, 464, 399
- Heavens A. F., Jimenez R., Lahav O., 2000, *MNRAS*, 317, 965
- Heavens A. F., Sellentin E., de Mijolla D., Vianello A., 2017, *Monthly Notices of the Royal Astronomical Society*, 472, 4244
- Heymans C., et al., 2012, *Monthly Notices of the Royal Astronomical Society*, 427, 146
- Hikage C., et al., 2019, *Publications of the Astronomical Society of Japan*, 71, 43
- Hildebrandt H., et al., 2020, *Astronomy & Astrophysics*, 633, A69
- Hinshaw G., et al., 2013, *ApJS*, 208, 19
- Hirata C., Seljak U., 2003, *Monthly Notices of the Royal Astronomical Society*, 343, 459
- Hivon E., Górski K. M., Netterfield C. B., Crill B. P., Prunet S., Hansen F., 2002, *The Astrophysical Journal*, 567, 2
- Hunter J. D., 2007, *Computing in science & engineering*, 9, 90
- Ivezić v., et al., 2019, *Astrophys. J.*, 873, 111
- Jain B., Seljak U., White S., 2000, *The Astrophysical Journal*, 530, 547
- Jones E., Oliphant T., Peterson P., et al., 2001–, SciPy: Open source scientific tools for Python. <http://www.scipy.org/>
- Kacprzak T., et al., 2016, *Monthly Notices of the Royal Astronomical Society*, 463, 3653
- Kaiser N., Squires G., 1993, *The Astrophysical Journal*, 404, 441
- Laureijs R., Amiaux J., Arduini S., Auguères J. L., Brinchmann J., Cole R., et al., 2011, arXiv e-prints, p. arXiv:1110.3193
- Lewis A., 2013, *Physical Review D*, 87, 103529
- Li X., et al., 2022, *Publications of the Astronomical Society of Japan*, 74, 421
- Li X., et al., 2023, arXiv preprint arXiv:2304.00702
- Liu J., Madhavacheril M. S., 2019, *Physical Review D*, 99, 083508
- Liu X., et al., 2014a, arXiv preprint arXiv:1412.3683
- Liu X., Wang Q., Pan C., Fan Z., 2014b, *The Astrophysical Journal*, 784, 31
- Liu J., Petri A., Haiman Z., Hui L., Kratochvil J. M., May M., 2015, *Physical Review D*, 91, 063507
- Liu X., Yuan S., Pan C., Zhang T., Wang Q., Fan Z., 2023, *Monthly Notices of the Royal Astronomical Society*, 519, 594
- Longley E. P., et al., 2023, *Monthly Notices of the Royal Astronomical Society*, 520, 5016
- Loureiro A., et al., 2022, *Astronomy & Astrophysics*, 665, A56
- Lu T., Haiman Z., Li X., 2023, *Monthly Notices of the Royal Astronomical Society*, 521, 2050
- Madhavacheril M. S., et al., 2023, arXiv preprint arXiv:2304.05203
- Mandelbaum R., et al., 2018a, *Publications of the Astronomical Society of Japan*, 70, S25
- Mandelbaum R., et al., 2018b, *Monthly Notices of the Royal Astronomical Society*, 481, 3170
- Marques G. A., Liu J., Matilla J. M. Z., Haiman Z., Bernui A., Novaes C. P., 2019, *Journal of Cosmology and Astroparticle Physics*, 2019, 019
- Marques G. A., Liu J., Huffenberger K. M., Hill J. C., 2020, *The Astrophysical Journal*, 904, 182
- Marques G., et al., 2023, arXiv preprint arXiv:2306.17268
- Martinet N., et al., 2018, *Monthly Notices of the Royal Astronomical Society*, 474, 712
- Martinet N., Castro T., Harnois-Déraps J., Jullo E., Giocoli C., Dolag K., 2021, *Astronomy & Astrophysics*, 648, A115
- Munshi D., Jain B., 2000, *MNRAS*, 318, 109
- Nelson D., et al., 2019, *Computational Astrophysics and Cosmology*, 6, 1
- Nishimichi T., et al., 2009, *Publications of the Astronomical Society of Japan*, 61, 321
- Oguri M., et al., 2018, *Publications of the Astronomical Society of Japan*, 70, S26
- Oliphant T. E., 2015, USA: CreateS-pace Independent Publishing Platform
- Osato K., Liu J., Haiman Z., 2021, *Monthly Notices of the Royal Astronomical Society*, 502, 5593
- Pérez F., Granger B. E., 2007, *Computing in Science & Engineering*, 9, 21
- Petri A., Liu J., Haiman Z., May M., Hui L., Kratochvil J. M., 2015, *Phys. Rev. D*, 91, 103511
- Pillepich A., et al., 2018, *Monthly Notices of the Royal Astronomical Society*, 475, 648
- Pires S., Starck J.-L., Amara A., Teyssier R., Réfrégier A., Fadili J., 2009, *Monthly Notices of the Royal Astronomical Society*, 395, 1265
- Price-Whelan A. M., et al., 2018, *AJ*, 156, 123
- Qu F. J., et al., 2023, arXiv preprint arXiv:2304.05202
- Sato M., Hamana T., Takahashi R., Takada M., Yoshida N., Matsubara T., Sugiyama N., 2009, *The Astrophysical Journal*, 701, 945
- Secco L. F., et al., 2022, *Physical Review D*, 105, 023515
- Semboloni E., Schrabback T., van Waerbeke L., Vafaei S., Hartlap J., Hilbert S., 2010, *Monthly Notices of the Royal Astronomical Society*, 410, 143
- Shan H., et al., 2018, *Monthly Notices of the Royal Astronomical Society*, 474, 1116
- Shirasaki M., Yoshida N., 2014, *The Astrophysical Journal*, 786, 43
- Shirasaki M., Yoshida N., Hamana T., 2013, *The Astrophysical Journal*, 774, 111
- Shirasaki M., Hamana T., Takada M., Takahashi R., Miyatake H., 2019, *Monthly Notices of the Royal Astronomical Society*, 486, 52
- Shirasaki M., Moriwaki K., Oogi T., Yoshida N., Ikeda S., Nishimichi T., 2021, *Monthly Notices of the Royal Astronomical Society*, 504, 1825
- Spergel D., et al., 2015, arXiv preprint arXiv:1503.03757
- Starck J.-L., Themelis K. E., Jeffrey N., Peel A., Lanusse F., 2021, *Astronomy & Astrophysics*, 649, A99
- Takada M., Jain B., 2003, *Monthly Notices of the Royal Astronomical Society*, 344, 857
- Takahashi R., Sato M., Nishimichi T., Taruya A., Oguri M., 2012, *The Astrophysical Journal*, 761, 152
- Takahashi R., Hamana T., Shirasaki M., Namikawa T., Nishimichi T., Osato K., Shiroyama K., 2017, *The Astrophysical Journal*, 850, 24
- Tanaka M., et al., 2018, *Publications of the Astronomical Society of Japan*, 70, S9
- Thiele L., Marques G. A., Liu J., Shirasaki M., 2023, arXiv preprint arXiv:2304.05928
- Torrado J., Lewis A., 2019, *Astrophysics Source Code Library*, pp ascl–1910
- Uhlemann C., Friedrich O., Boyle A., Gough A., Barthelemy A., Bernardeau F., Codis S., 2023, *The Open Journal of Astrophysics*, 6, 1
- Valageas, P. Nishimichi, T. 2011, *A&A*, 527, A87
- White M., et al., 2022, *Journal of Cosmology and Astroparticle Physics*, 2022, 007
- Zürcher D., et al., 2022, *Monthly Notices of the Royal Astronomical Society*, 511, 2075

APPENDIX A: EMULATOR ACCURACY

We test the accuracy of the emulator by doing the “leaving-one-out” validation. We built the emulator by removing each of the 100 cosmologies at each turn and checked how well this removed cosmology can be recovered. Figs. [A1](#) and [A2](#) show the mean residual values for the Peak counts (upper panel), Minima (middle panel), and Power spectrum (lower panel), for maps smoothed with 4 and 8 arcmin, respectively. We found that the relative residual of the emulator does not exceed $\sim 4\%$ within the prior range, enabling unbiased estimation in our analysis.

This paper has been typeset from a $\text{\TeX}/\text{\LaTeX}$ file prepared by the author.

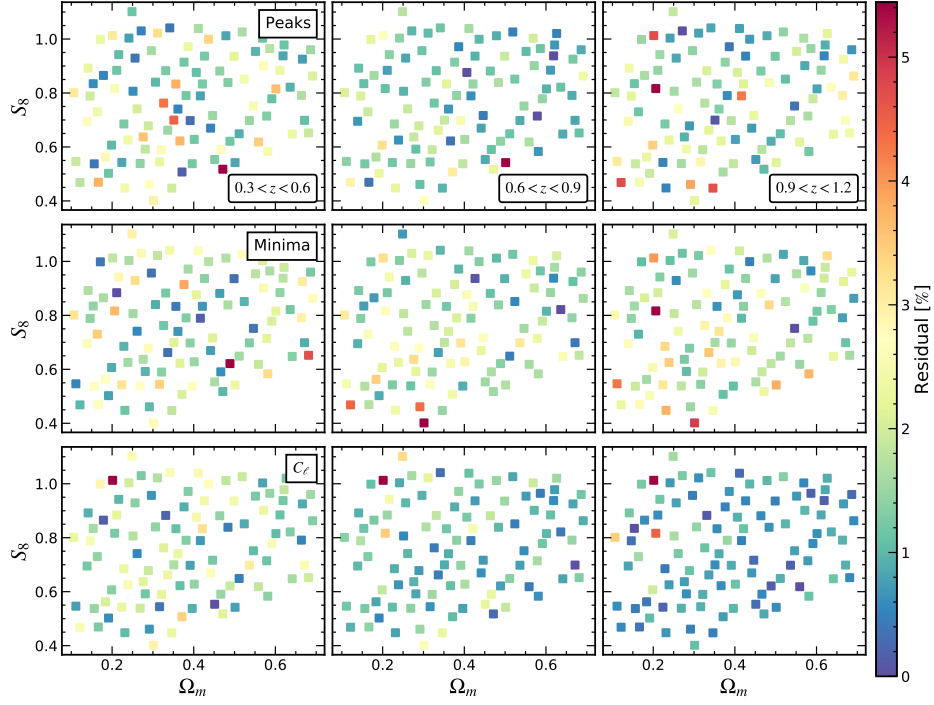


Figure A1. “Leave-one-out” validation of the Gaussian Process emulator for the Peak Counts (upper panel), minimum counts (middle panel), and Power Spectrum (lower panel) of each tomographic bin and considering maps smoothed with smoothing scale equal to 4 arcmin. The emulator is built by removing the simulations at each cosmology, and then we compare the prediction with the true data that was removed. The colors denote the amplitude, in percentage, of the mean relative residual.

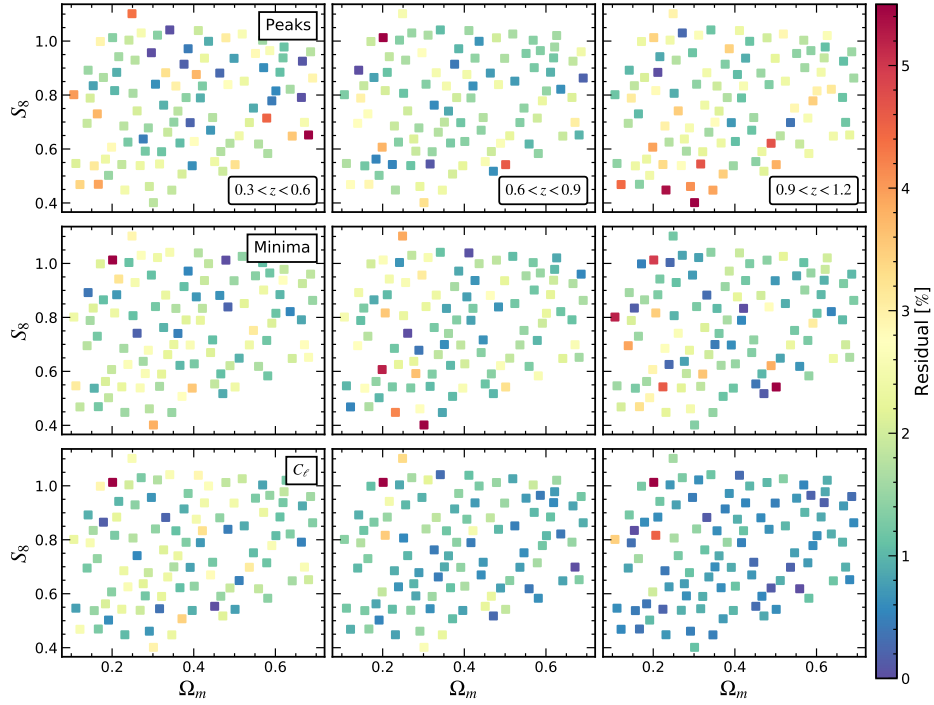


Figure A2. The same as Fig. A1, but for maps smoothed with smoothing scale equal to 8 arcmin.